

Strategy of extra Zr doping on the enhancement of thermoelectric performance for TiZr_xNiSn synthesized by a modified solid-state reaction

Jun-Liang Chen

Guangxi University

Hengquan Yang

Huaiyin Normal University

Chengyan Liu

Guilin University of Technology

Jisheng Liang

Guangxi University

Lei Miao (✉ miaolei@guet.edu.cn)

Guilin University of Electronic Technology <https://orcid.org/0000-0002-2281-2689>

Zhongwei Zhang

Guilin University of Technology

Pengfei Liu

Shibaura Institute of Technology College of Systems Engineering and Science: Shibaura Kogyo Daigaku System Riko Gakubu

Kenta Yoshida

Shibaura Institute of Technology College of Systems Engineering and Science: Shibaura Kogyo Daigaku System Riko Gakubu

Chen Chen

Harbin Institute of Technology School of Materials Science and Engineering

Qian Zhang

Harbin Institute of Technology School of Materials Science and Engineering

Qi Zhou

Guangxi University

Yuntiao Liao

Guangxi University

Ping Wang

Guangxi University

Zhixia Li

Guangxi University

Biaolin Peng

Research Article

Keywords: thermoelectric, half-Heusler, extra Zr doped TiNiSn, solid-state reaction

Posted Date: July 24th, 2021

DOI: <https://doi.org/10.21203/rs.3.rs-736846/v1>

License:  This work is licensed under a Creative Commons Attribution 4.0 International License.

[Read Full License](#)

Abstract

Half-Heusler alloys, which possess the advantages of high thermal stability, large power factor and good mechanical property, have been attracted increasing interest in mid-temperature thermoelectric application. In this work, the extra Zr-doped TiZr_xNiSn samples were successfully prepared by a modified solid-state reaction followed by spark plasma sintering. It demonstrates that extra Zr doping could not only improve the power factor on account of an increase in Seebeck coefficient but also suppress the lattice thermal conductivity originated from the strengthened phonon scattering by the superlattice nanodomains and the secondary nanoparticles. As a consequence, an increased power factor of $3.29 \text{ mW m}^{-1} \text{ K}^{-2}$ and a decreased lattice thermal conductivity of $1.74 \text{ W m}^{-1} \text{ K}^{-1}$ are achieved in $\text{TiZr}_{0.015}\text{NiSn}$, leading to a peak ZT as high as 0.88 at 773 K and an average ZT value up to 0.62 in the temperature range of 373 – 773 K. This work gives a guidance for optimizing the thermoelectric performance of TiNiSn -based alloys by modulating the microstructures on the secondary nanophases and superlattice nanodomains.

1 Introduction

Thermoelectric (TE) materials can directly convert heat into electricity, *i.e.*, the carrier density gradient causes the diffusion of the carriers (electrons and holes) from the hot to the cold end of a semiconductor, and an electric potential difference would be built up against this process, having bright prospects in the low-grade waste heat recovery [1 – 3]. The energy conversion efficiency of thermoelectric materials is usually tailored by the dimensionless figure of merit (ZT), $ZT = S^2 \sigma \kappa^{-1} T$, where T is the absolute temperature, S is the Seebeck coefficient, σ is the electrical conductivity, $S^2 \sigma$ is the power factor (PF), κ is the total thermal conductivity, which is usually comprised of the electronic (κ_e) and lattice (κ_l) thermal conductivity. Theoretically, an outstanding thermoelectric material should simultaneously possess a high S , a high σ , as well as a low κ [4].

Many excellent thermoelectric materials have been developed in recent decades, including half-Heusler (HH) alloys [5, 6], chalcogenides [7, 8], pentatellurides [9] and phonon glass electron crystal (PGEC) (*e.g.*, skutterudites and clathrates) [10, 11]. Among them, the HH alloys exhibit excellent mechanical property, good thermal stability and relatively abundant non-toxic raw materials [12], making them an attractive candidate for mid-temperature thermoelectric application. MNiSn ($M = \text{Ti, Zr, Hf}$) alloy, which has a cubic MgAgAs -type structure (space group: $F4\bar{3}m$), belongs to a class of intermetallic compound with an indirect band gap in the range of 0.1 – 0.5 eV [13]. Such HH alloy usually exhibits a high σ and an intermediate S , which result in a relatively large PF [14, 15]. However, the high thermal conductivity (*e.g.*, $\sim 10 \text{ W m}^{-1} \text{ K}^{-1}$ at room temperature [16]) is one of the biggest disadvantages for half-Heusler alloys as a thermoelectric material candidate [17]. Therefore, various strategies, such as boundary phonon scattering [18, 19], nanostructures [20], and multi-scale scattering [21], were employed to reduce the κ_l by strengthening the phonon scattering. For example, Rabin *et al.* reported that the mass-fluctuations caused by Al doping could effectively reduce the κ_l to $3.1 \text{ W m}^{-1} \text{ K}^{-1}$ at 703 K ($\text{Ti}_{0.99}\text{Al}_{0.01}\text{NiSn}$) [14]. Schrade *et*

al. reported that both ultrafine grains (≤ 100 nm) and defects can play an important role in the reduction of κ_l , also leading a low κ_l of $3.1 \text{ W m}^{-1} \text{ K}^{-1}$ at 625 K for TiNiSn [22].

Up to now, many methods have been employed to synthesize MNiSn (M = Ti, Zr, Hf) alloys, such as arc melting [23], levitation melting [24], solid-state reaction [25], microwave method [26], mechanical alloying [27]. However, it is difficult to synthesize the pure phase of half-Heusler alloys TiNiSn directly, which shows a narrow phase stability window according to the TiNiSn phase diagram [28]. The Sn element would first melt and react with other elements during the synthesis process, due to its low melting point (505 K), leading to the aggregation of elemental Sn and the generation of related impurities (Ti_6Sn_5 , TiNi_2Sn), which usually needs a long time annealing (2 weeks) to eliminate [29]. Nonetheless, Ren *et al.* have been demonstrated that pure phase TiNiSn could be prepared by means of arc melting, ball milling followed by hot pressing [30]. Herein, we describe a modified solid-state reaction method for synthesizing the TiNiSn-based TE materials. The solid-state reaction usually conducts at relatively low temperatures, so that the experimental conditions are readily satisfied and has the virtues of energy-saving and good repeatability, which is conducive to industrial production.

In this work, Zr-doped TiNiSn alloys have been successfully prepared by a modified solid-state reaction followed by spark plasma sintering (SPS). It demonstrates that extra Zr doping is effective in improving the thermoelectric properties compared to the substitution of Ti with nominal stoichiometry Zr, as shown in Fig. S1. Therefore, this paper mainly focuses on the effect of extra Zr doping on the thermoelectric properties of TiNiSn. Compared with the pristine TiNiSn, the power factor is improved by 1.5 times and the lattice thermal conductivity is suppressed by 34% in the sample $\text{TiZr}_{0.015}\text{NiSn}$, leading to a peak ZT value of 0.88 at 773 K and an average ZT value of 0.62 in the temperature range of 373 – 773 K. This work demonstrates extra Zr doping is an effective strategy to optimize the thermoelectric performance of TiNiSn-based materials, and offers enlightenment and reference to the relevant materials.

2 Experiment Procedure

2.1 Synthesis

Ti (99.9%, Aladdin), Zr (99.5%, Aladdin), Ni (99.9%, Aladdin), Sn (99.9%, Aladdin) powders were weighed according to the nominal compositions of TiZr_xNiSn ($x = 0, 0.005, 0.015, 0.025$). For a typical synthesis process, the powders were firstly mixed and cold-pressed into a block, and then it was wrapped up by the carbon paper and buried in silicon carbide powder in a corundum crucible. The solid-state reaction was conducted in three steps: maintained (1) at 473 K for 10 h, (2) at 973 K for 10 h, and (3) at 1173 K for 24 h under Ar/H_2 atmosphere in a tube furnace. The synthesized samples were pulverized using an agate mortar pestle and then the obtained powders were sintered into bulk samples by the SPS technique (LABOX-325, SINTER LAND INC.) at 1173 K for 4 min under an axial pressure of 50 MPa in vacuum.

2.2 Characterization

X-ray diffraction (XRD, Bruker D8 Advance, Germany, Cu K α radiation, $\lambda = 0.154$ nm) was used to characterize the phase composition and crystal structure of the sample. The microstructures were observed by the field-emission scanning electron microscope (FE-SEM, Zeiss Sigma 500, Germany) and transmission electron microscopy (TEM, JEOL ARM 200F, Japan), the composition was analysed by energy disperse spectroscopy (EDS, Oxford X-Max^N, England). The electrical conductivity and Seebeck coefficient were measured by a model CTA-3 thermoelectric parameter test system (Beijing Cryoall Science and Technology Co., Ltd, China) in the helium (99.999%) atmosphere. The Hall coefficient (R_H) was evaluated by using the van der Pauw technique under a reversible magnetic field of 1.5 T. The hall carrier concentration (n) and mobility (μ) were calculated by formulas $n = 1/(eR_H)$ and $\mu = R_H/\rho$, respectively. The thermal conductivity is calculated by the formula $\kappa = DdC_p$, where D is the thermal diffusivity measured by the laser flash method (Netzsch LFA467 HT, Germany), C_p is the specific heat capacity of the material measured by the contrast method (Netzsch LFA467 HT, Germany), d is the density measured by Archimedes' method, all the samples show a high relative density, higher than 95% (Table 1).

Table 1

Lattice parameters, density and relative density of the Zr-doped TiNiSn samples

Samples	Lattice parameters (Å)	Density (g cm ⁻³)	Relative density (%)
TiNiSn	5.933	6.902	96.53
TiZr _{0.005} NiSn	5.939	6.869	96.07
TiZr _{0.015} NiSn	5.940	6.825	95.45
TiZr _{0.025} NiSn	5.948	6.897	96.46

3 Results And Discussion

The crystal structure of TiNiSn belongs to a cubic system, where each kind of atom forms a face centered cubic lattice, as shown in Fig. 1a. The XRD patterns of the synthesized TiZr_xNiSn samples are presented in Fig. 1b, which shows the main diffraction peaks of all the samples could be indexed to the cubic phase TiNiSn (reference code: 03 - 065 - 0617), suggesting the samples could be successfully prepared by the modified solid-state reaction. Besides, a few weak peaks corresponding to TiNi₂Sn, ZrNiSn, Sn₅Ti₆ and Sn were detected. The enlarged XRD patterns in the 2 θ range of 42°–44° clearly show the low-angle shifting of major diffraction peak, (220) plane, with increasing Zr content, which is possibly due to the incorporation of the larger ions Zr⁴⁺ (inradius: 72 pm) into the Ti⁴⁺ (inradius: 53 pm) sublattice. As expected, Zr doping leads to a slight expansion of the unit cell, see the calculated lattice parameters in Table 1. And,

the smaller electronegativity of Zr (1.33) compared with Ti (1.54) could lead to an increase in the bonding force, making the crystal structure more stable.

Figure 2 and S2 show the SEM images of freshly fractured surface for TiZr_xNiSn ($x = 0, 0.005, 0.015, 0.025$) samples. It can be seen that each bulk sample is comprised of the compacted grains, which is consistent with its high relative density. Notably, the size of the grains in the pristine sample TiNiSn ($x = 0$) is on micrometer scale (Fig. 2a). Notably, as the Zr amount increases to $x = 0.015$, there appear many nanoparticles in the matrix (Fig. 2c), which is conducive to reducing the κ_f of the materials. Fig. S3 is the local particle size statistics of $\text{TiZr}_{0.015}\text{NiSn}$. It can be seen that the particle diameter in this region ranges from 25nm to 726nm, of which 79.5% is less than 100 nm, and the average grain size is 83.7nm. To further clarify the composition of these nanoparticles, EDS mapping was carried out on the typical sample $\text{TiZr}_{0.015}\text{NiSn}$, as shown in Fig. S4. It shows that the aggregation area of Zr and Sn is exactly corresponded to the nanoparticles accumulated zone, suggesting that these nanoparticles are in (Zr, Sn)-rich phase.

As shown in Fig. 3, TEM and HRTEM characterizations are performed on the pristine TiNiSn and $\text{TiZr}_{0.015}\text{NiSn}$ samples. Figure 3b shows a HRTEM image of the pristine TiNiSn sample taken from the marked area in Fig. 3a. It can be seen that the clear lattice fringes corresponding to $(0\bar{2}0)$ plane spread over a large area (> 20 nm), showing a good crystallinity of the pristine sample. In contrast, as observed in Fig. 3d, there are nanodomains with a size of ~ 15 nm in the $\text{TiZr}_{0.015}\text{NiSn}$ matrix, which has a superlattice structure with the characteristic plane spacing of 8.66 \AA , as it is coincident about 3 times of lattice spacings of plane $(0\bar{2}0)$, 2.94 \AA . We confirmed that these nanodomains are uniquely dispersing in the current $\text{TiZr}_{0.015}\text{NiSn}$ matrix, as shown at black arrowed points in Fig. 4c by using HRTEM technique. Such nanodomains might also play an important role in suppressing the κ_f .

Figure 4a plots the temperature-dependent n of the samples TiZr_xNiSn ($x = 0, 0.005, 0.015, 0.025$), which shows a decrease trend with the increase of Zr content. It is demonstrated that the impurity of residual elemental Sn could increase the n in TiNiSn [15, 31]. Conversely, the residual Sn in TiNiSn is diminished with the increase of Zr content (Fig. 1b), which could contribute a decrease in the n .

Figure 4b plots the temperature-dependent μ of the samples TiZr_xNiSn , which shows an increase trend with the increase of Zr content. This could be ascribed to the significant decrease in n and the change of carrier scattering mechanism [32]. For the TiNiSn with nominal Zr content at $x = 0$ and 0.005 , the carrier mobility is divided into two regions over the temperature range of $300 - 720$ K. When the temperature is lower than 500 K, the mobility increases with rising the temperature, suggesting the scattering of ionized impurity is dominant. When the temperature above 500 K, the temperature-dependent μ obeys $T^{-0.5}$ law, which indicates that the alloy scattering is dominant, which is basically consistent with the literatures [33].

Figure 5 shows the temperature-dependent electrical properties of the samples TiZr_xNiSn ($x = 0, 0.005, 0.015, 0.025$). Figure 5a demonstrates that the σ of the TiZr_xNiSn samples increases with rising temperature, for the typical sample $\text{TiZr}_{0.015}\text{NiSn}$, which is from 342 S cm^{-1} at 323 K to 914 S cm^{-1} at 823 K. And the electrical conductivity shows a decreasing tendency with increasing the Zr content, which decreases from 611 S cm^{-1} for the pristine sample to 274 S cm^{-1} for the sample $\text{TiZr}_{0.025}\text{NiSn}$ at room temperature, which is consistent with the change of carrier concentration. Additionally, it is confirmed that the Sn-rich metallic phase could result in the increase of σ , as shown in Fig. S5. Notably, the jump region in the temperature-dependent σ curve (marked in yellow) could be attributed to the elemental Sn resided in the matrix, which has a low melting point (505 K).

The temperature-dependent S of the TiZr_xNiSn samples are plotted in Fig. 5b. The negative value indicates an n -type conducting behavior of TiZr_xNiSn samples. From the Goldsmid formula [37], the band gap can be estimated by the maximum Seebeck coefficient and its corresponding temperature. It is found that Zr doping can improve the band gap from 0.19 eV to 0.25 eV. With rising temperature ($> 526 \text{ K}$), the decrease of the absolute value of S for all samples could be attributed to the bipolar diffusion effect at high temperatures. Additionally, it can be seen that the absolute value of S increases with increasing the Zr content, which is mainly due to the decrease in n . For a degenerate semiconductor, the S is commonly correlated with n , which could be described by the Mott equation [38], *i.e.*,

$$S = \pm \frac{8\pi^2 k_B^2}{3eh^2} m^* T \left(\frac{\pi}{3n}\right)^{\frac{2}{3}},$$

where k_B is the Boltzmann constant, h is the Planck constant, m^* is the carrier density of states effective mass, and e is the elemental charge.

Furthermore, the S as a function of n at 323 K, together with Pisarenko curve based on the single parabolic model using $m^* = 1.52 m_e$ is plotted in Fig. 5c. For the samples with $x = 0$ and 0.005, the absolute S agrees well with the fitted curve, while the absolute S for $x = 0.015$ and 0.025 samples locates below the curve, indicating the decrease in m^* , which is consistent with the increase of μ (Fig. 4b). With both decrease in n and m^* , it reaches a conclusion that the enhanced absolute S for Zr-doped samples is due to the decline in n according to the Mott equation. As expected, the maximum absolute value of S up to $207 \mu\text{V K}^{-1}$ at 538 K is attained in the $\text{TiZr}_{0.015}\text{NiSn}$ sample.

Figure 5d shows the temperature-dependent PF of the samples TiZr_xNiSn . The power factor is significantly improved in Zr doped samples due to the significant enhancement of S . The maximum power factor of $3.29 \text{ mW m}^{-1} \text{ K}^{-2}$ at 773 K is achieved in the sample $\text{TiZr}_{0.015}\text{NiSn}$, which is 50% higher than that value of the pristine TiNiSn sample, and comparable to the Mn-doped TiNiSn [15].

Figure 6a shows the κ of TiZr_xNiSn ($x = 0, 0.005, 0.015, 0.025$) samples. We can see that the pristine sample exhibits a high κ , $3.9 - 4.4 \text{ W m}^{-1} \text{ K}^{-1}$ in the temperature range of 323 - 823 K. And extra Zr doping could effectively reduce the κ of the TiNiSn -based material, as demonstrated in the doped samples. The lowest κ is obtained in the sample $\text{TiZr}_{0.015}\text{NiSn}$, which is $2.3 \text{ W m}^{-1} \text{ K}^{-1}$ at 573 K. To

clarify the reasons, we calculated the κ_e ($\kappa_e = L\sigma T$, where L is the Lorentz number determined by fitting the measured S based on the single parabolic band model [39, 40], as shown in Fig. S6c) and the κ_l ($\kappa_l = \kappa - \kappa_e$), which are plotted in Fig. S6d and Fig. 6b, respectively. It shows that the κ is mainly contributed by the κ_l , especially at low temperatures (< 600 K). Also the decrease in κ for the Zr-doped samples is mainly contributed by the reduction of κ_l . The minimum κ_l as low as $1.74 \text{ W m}^{-1} \text{ K}^{-1}$ at 723K is attained in the $\text{TiZr}_{0.015}\text{NiSn}$. In order to further understand the contribution of various phonon scattering sources on the reduction of κ_l , the Debye-Callaway model is employed [41]. The solid line is the theoretical κ_l with respect to mass and strain fluctuation caused by Zr substitution on Ti sites. As shown in Fig. 6c, the experimental κ_l is significantly lower than the theoretical curve, suggesting the reduction of κ_l is originated from other phonon scattering sources. According to the XRD, SEM, and TEM characterization results, it is believed that the secondary nanoparticles and superlattice-like nanodomains may be responsible for the low κ_l in $\text{TiZr}_{0.015}\text{NiSn}$.

Figure 7a shows the temperature-dependent ZT of the samples TiZr_xNiSn over 323 – 823 K, which are greatly improved by extra Zr doping. The maximum ZT value of 0.88 at 773 K is achieved in $\text{TiZr}_{0.015}\text{NiSn}$, which is more than twice that value of the pristine sample. The average ZT value is

$$ZT_{\text{avg}} = \frac{1}{T_h - T_c} \int_{T_c}^{T_h} ZT dT,$$

calculated using the formula, where T_c and T_h are the temperatures of the cold and hot end, respectively, ZT_{avg} is the ratio between integrated area under the ZT curve and temperature difference $\Delta T = T_h - T_c$. The average ZT value obtained in the sample $\text{TiZr}_{0.015}\text{NiSn}$ is up to 0.62 in the temperature range of 373–773 K, which is much higher than the reported values of the counterparts [14,15,24,42–44].

4 Conclusion

In summary, Zr-doped TiNiSn samples were successfully prepared by a modified solid-state reaction combined with SPS technology. Extra Zr doping not only leads to an obviously improved power factor but also results in a greatly suppressed lattice thermal conductivity due to the appearance of a lot of nanoparticles and superlattice nanodomains. For a typical sample $\text{TiZr}_{0.015}\text{NiSn}$, the power factor increases by 50%, and the thermal conductivity decreases by 40% compared with the pristine TiNiSn , as a result, a peak ZT of 0.88 at 780 K and an average ZT up to 0.62 in the temperature range of 373 – 773 K are obtained. This work could give a guidance for optimizing the thermoelectric performance of relevant materials by regulating the microstructures such as superlattice-like nanodomains.

Declarations

Declaration of competing interest

The authors declare that they have no known competing financial interests or personal relationships that could have appeared to influence the work reported in this paper.

Acknowledgment

This work was supported by the National Key Research and Development Program of China (No. 2017YFE0198000), National Natural Science Foundation of China (Grant No. 51772056, 51801040), Guangxi Natural Science Foundation of China (Grant No. 2020GXNSFAA159111, AD20159006) and Japan Society for the Promotion of Science (20K22486).

References

1. Ebrahimi K, Jones GF, Fleischer AS (2014) A review of data center cooling technology, operating conditions and the corresponding low-grade waste heat recovery opportunities. *Renew Sust Energy Rev* 31:622–638
2. Bell LE (2008) Cooling, heating, generating power, and recovering waste heat with thermoelectric systems. *Science* 321:1457–1461
3. Zhang YL, Cleary M, Wang XW et al (2015) High-temperature and high-power-density nanostructured thermoelectric generator for automotive waste heat recovery. *Energy Convers Manage* 105:946–950
4. Zeier WG, Zevalkink A, Gibbs ZM et al (2016) Thinking Like a Chemist: Intuition in Thermoelectric Materials. *Angew Chem Int Edit* 55:6826–6841
5. Pedersen SV, Croteau JR, Kempf N et al (2020) Novel synthesis and processing effects on the figure of merit for NbCoSn, NbFeSb, and ZrNiSn based half-Heusler thermoelectrics. *J Solid State Chem* 285:121203
6. Dasmahapatra A, Daga LE, Karttunen AJ et al (2020) Key Role of Defects in Thermoelectric Performance of TiMSn (M = Ni, Pd, and Pt) Half-Heusler Alloys. *J Phys Chem C* 124:14997–15006
7. Liu CY, Huang ZW, Wang DH et al (2019) Dynamic Ag⁺-intercalation with AgSnSe₂ nano-precipitates in Cl-doped polycrystalline SnSe₂ toward ultra-high thermoelectric performance. *J Mater Chem A* 7:9761–9772
8. Zhao LD, Lo SH, Zhang YS et al (2014) Ultralow thermal conductivity and high thermoelectric figure of merit in SnSe crystals. *Nature* 508:373–377
9. Shi XL, Ai X, Zhang QH et al (2020) Enhanced thermoelectric properties of hydrothermally synthesized n-type Se&Lu-codoped Bi₂Te₃. *J Adv Ceram* 9:424–431
10. Kim SW, Kimura Y, Mishima Y (2004) Enhancement of high temperature thermoelectric properties of intermetallic compounds based on a Skutterudite IrSb₃ and a half-Heusler TiNiSb. *Sci Technol Adv Mat* 5:485–489
11. Mei J, Yao Z, Zhu SY et al (2019) Step distribution of Yb filling fraction during microstructural evolution in skutterudites. *J Adv Ceram* 8:62–71

12. Chen S, Ren ZF (2013) Recent progress of half-Heusler for moderate temperature thermoelectric applications. *Mater Today* 16:387–395
13. Ogut S, Rabe KM (1995) Band gap and stability in the ternary intermetallic compounds NiSnM (M = Ti, Zr, Hf): A first-principles study. *Phys Rev B* 51:10443–10453
14. Rabin D, Kyratsi T, Fuks D et al (2020) Thermoelectric transport properties of $(\text{Ti}_{1-c}\text{Al}_c)\text{NiSn}$ half-Heusler alloy. *Phys Chem Chem Phys* 22:1566–1574
15. Lkhagvasuren E, Ouardi S, Fecher GH et al (2017) Optimized thermoelectric performance of the n-type half-Heusler material TiNiSn by substitution and addition of Mn. *AIP Adv* 7:045010
16. Hohl H, Ramirez AP, Goldmann C et al (1999) Efficient dopants for ZrNiSn-based thermoelectric materials. *J phys Condens matter* 11:1697–1709
17. Zhu TJ, Fu CG, Xie HH et al (2015) High Efficiency Half-Heusler Thermoelectric Materials for Energy Harvesting. *Adv Energy Mater* 5:1500588
18. Moon H, Kim J, Chun DW et al (2020) Radial heterostructure and interface effects on thermoelectric transport properties of Bi/Sn and Bi/Sb core/shell nanowires. *Curr Appl Phys* 20:43–48
19. Rausch E, Balke B, Ouardi S et al (2014) Enhanced thermoelectric performance in the p-type half-Heusler $(\text{Ti}/\text{Zr}/\text{Hf})\text{CoSb}_{0.8}\text{Sn}_{0.2}$ system via phase separation. *Phys Chem Chem Phys* 16:25258–25262
20. He R, Zhu TS, Wang YM et al (2020) Unveiling the phonon scattering mechanisms in half-Heusler thermoelectric compounds. *Energy Environ Sci*. DOI:10.1039/D0EE03014G
21. Biswas K, He JQ, Blum ID et al (2012) High-performance bulk thermoelectrics with all-scale hierarchical architectures. *Nature* 489:414–418
22. Schrade M, Berland K, Eliassen S et al (2017) The role of grain boundary scattering in reducing the thermal conductivity of polycrystalline XNiSn (X = Hf, Zr, Ti) half-Heusler alloys. *Sci Rep* 7:370–376
23. Bae KW, Hwang JY, Kim S et al (2020) Thermoelectric Transport Properties of n-Type Sb-doped (Hf, Zr, Ti)NiSn Half-Heusler Alloys Prepared by Temperature-Regulated Melt Spinning and Spark Plasma Sintering. *Appl Sci* 10:4936
24. Liu YT, Xie HH, Fu CG et al (2015) Demonstration of a phonon-glass electron-crystal strategy in (Hf, Zr)NiSn half-Heusler thermoelectric materials by alloying. *J Mater Chem A* 3:22716–22722
25. Chen JL, Liu CY, Miao L et al (2017) Improved Thermoelectric Performance Achieved by Regulating Heterogeneous Phase in Half-Heusler TiNiSn-Based Materials. *J Electron Mater* 47:3248–3253
26. Birkel CS, Zeier WG, Douglas JE et al (2012) Rapid Microwave Preparation of Thermoelectric TiNiSn and TiCoSb Half-Heusler Compounds. *Chem Mater* 24:2558–2565
27. Karati A, Murty BS (2017) Synthesis of nanocrystalline half-Heusler TiNiSn by mechanically activated annealing. *Mater Lett* 205:114–117
28. Gürth M, Grytsiv A, Vrestal J et al. On the constitution and thermodynamic modelling of the system Ti–Ni–Sn. *RSC Adv* 2015, 5: DOI:10.1039/C5RA16074J

29. Katayama T, Kim SW, Kimura Y et al (2003) The effects of quaternary additions on thermoelectric properties of TiNiSn-based half-Heusler alloys. *J Electron Mater* 32:1160–1165
30. Ren WY, Zhu HT, Mao J et al (2019) Manipulation of Ni Interstitials for Realizing Large Power Factor in TiNiSn-Based Materials. *Advanced Electronic Materials* 5:1900166
31. Peng Y, Miao L, Gao J et al (2019) Realizing High Thermoelectric Performance at Ambient Temperature by Ternary Alloying in Polycrystalline $\text{Si}_{1-x-y}\text{Ge}_x\text{Sn}_y$ Thin Films with Boron Ion Implantation. *Sci Rep* 9:14342
32. Makongo JPA, Misra DK, Zhou XY et al (2011) Simultaneous Large Enhancements in Thermopower and Electrical Conductivity of Bulk Nanostructured Half-Heusler Alloys. *J Am Chem Soc* 133:18843–18852
33. Xie HH, Wang H, Fu CG et al (2014) The intrinsic disorder related alloy scattering in ZrNiSn half-Heusler thermoelectric materials. *Sci Rep* 4:6888
34. Muta H, Kanemitsu T, Kurosaki K et al (2009) High-temperature thermoelectric properties of Nb-doped MNiSn (M = Ti, Zr) half-Heusler compound. *J Alloy Compd* 469:50–55
35. Tang YL, Li XS, Martin LHJ et al (2018) Impact of Ni content on the thermoelectric properties of Half-Heusler TiNiSn. *Energ Environ Sci* 11:311–320
36. Berry T, Fu CG, Auffermann G et al. Enhancing Thermoelectric Performance of TiNiSn Half-Heusler Compound via Modulation Doping. *Chem Mater* 2017, 29
37. Goldsmid HJ, Sharp JW (1999) Estimation of the thermal band gap of a semiconductor from Seebeck measurements. *J Electron Mater* 28:869–872
38. Snyder GJ, Toberer ES (2008) Complex thermoelectric materials. *Nat Mater* 7:105–114
39. Zhao LD, Lo SH, He JQ, Li H, Biswas K, Androulakis J et al (2011) High Performance Thermoelectrics from Earth-Abundant Materials: Enhanced Figure of Merit in PbS by Second Phase Nanostructures. *J Am Chem Soc* 133:20476–20487
40. Liu WS, Zhang QY, Lan YC et al (2011) Thermoelectric Property Studies on Cu-Doped n-Type $\text{Cu}_x\text{Bi}_2\text{Te}_{2.7}\text{Se}_{0.3}$ Nanocomposites. *Adv Energy Mater* 1:577–587
41. Abeles B (1963) Lattice thermal conductivity of disordered semiconductor alloys at high temperatures. *Phys Rev* 131:1906–1911
42. Li Y, Cheng C, Lei Y et al (2017) Ultra-fast preparation of high-performance thermoelectric bulk $\text{TiNiSb}_{0.05}\text{Sn}_{0.95}$ by microwave synthesis. *Dalton Trans* 46:33–38
43. Kimura Y, Ueno H, Kenjo T et al. Phase Stability and Thermoelectric Properties of Half-Heusler (Ma, Mb)NiSn (Ma, Mb = Hf, Zr, Ti). *Mrs Proceedings* 2008, **1128**: 1128–U01–09
44. Kim SW, Kimura Y, Mishima Y (2007) High temperature thermoelectric properties of TiNiSn-based half-Heusler compounds. *Intermetallics* 15:349–356

Figures

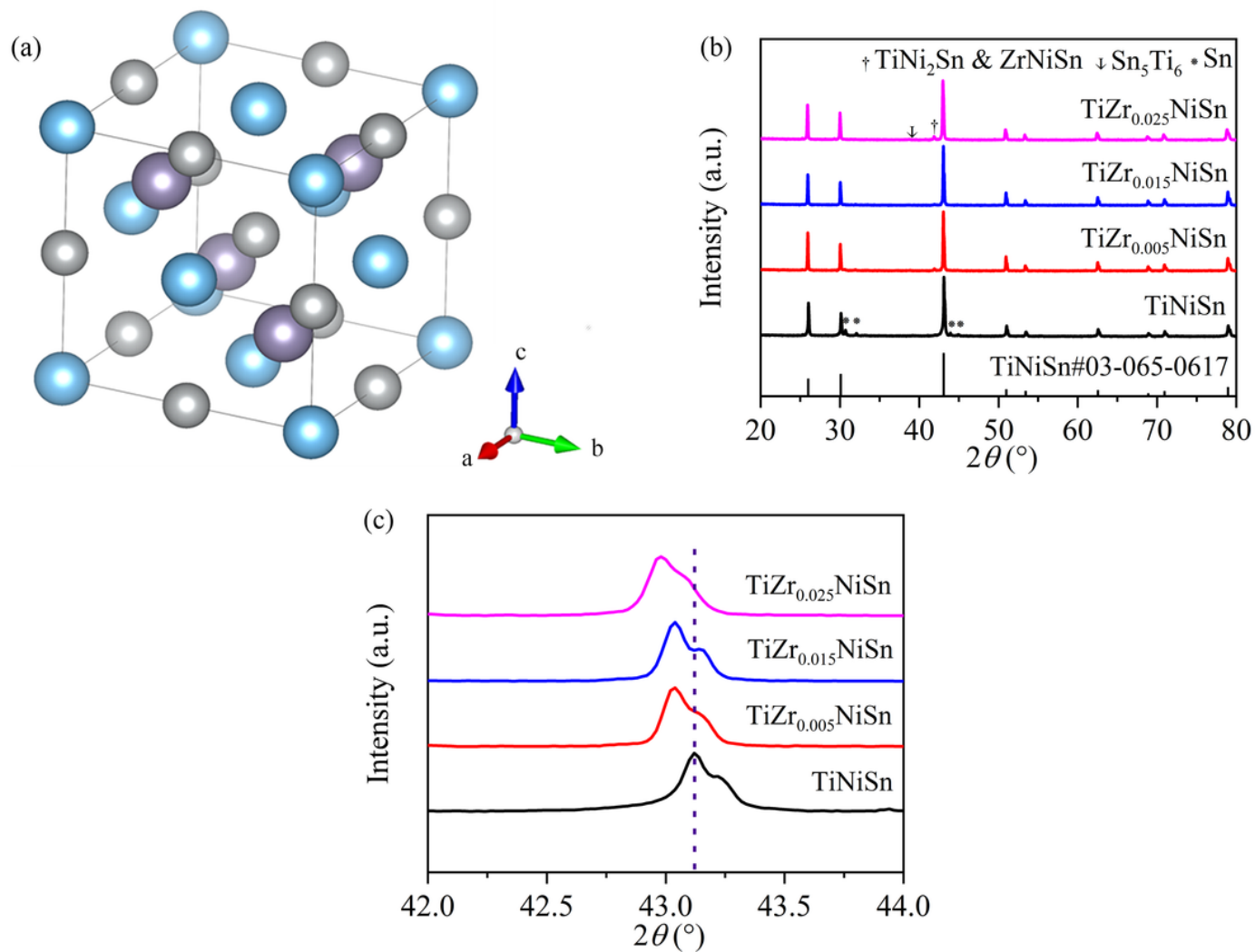


Figure 1

(a) Crystal structure of TiNiSn; (b) XRD patterns of the samples TiZr_xNiSn (x = 0, 0.005, 0.015, 0.025); (c) enlarged XRD patterns ranging from 42° to 44°.

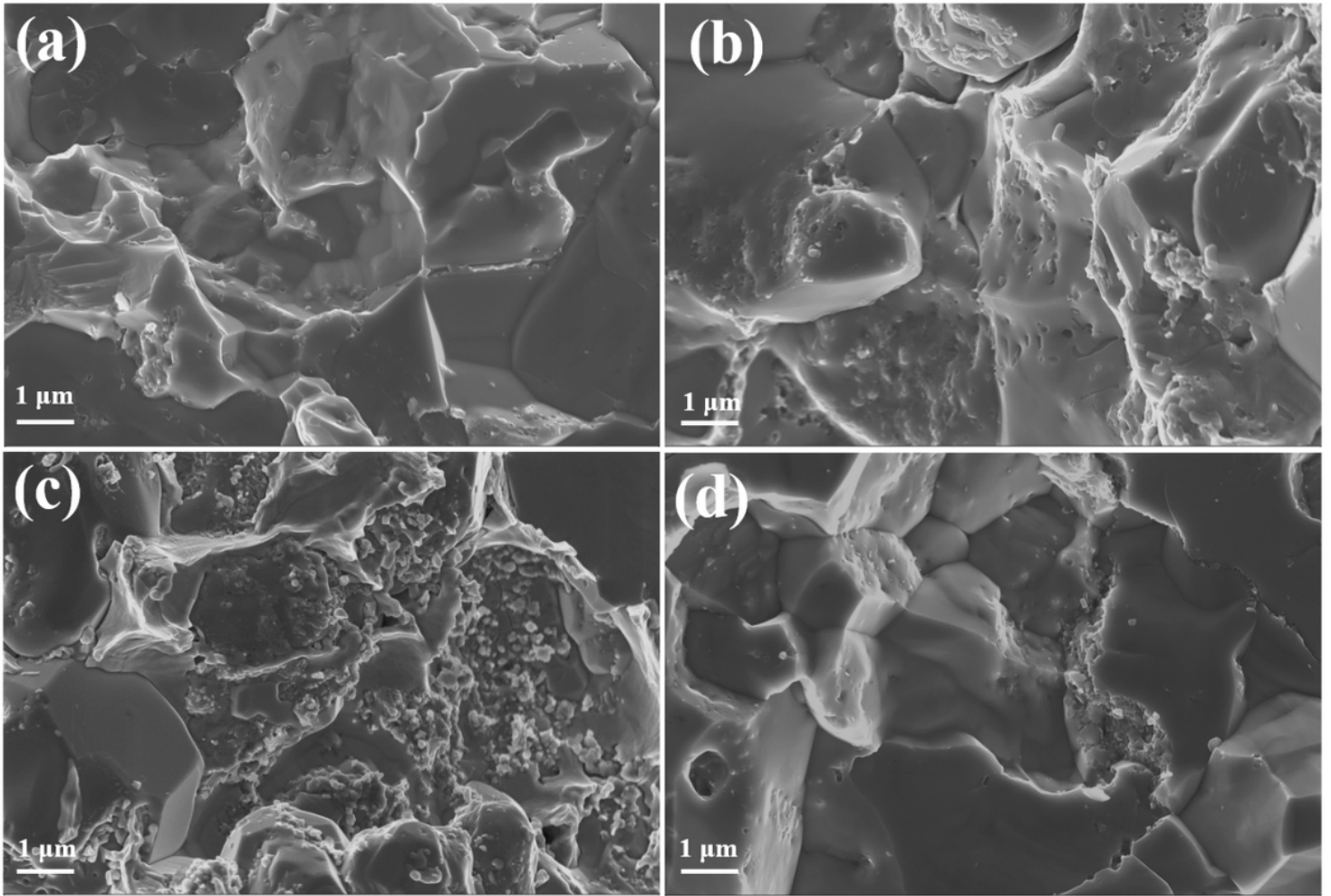


Figure 2

The SEM images of freshly fractured surface for TiZr_xNiSn samples: (a) $x = 0$; (b) $x = 0.005$; (c) $x = 0.015$; (d) $x = 0.025$.

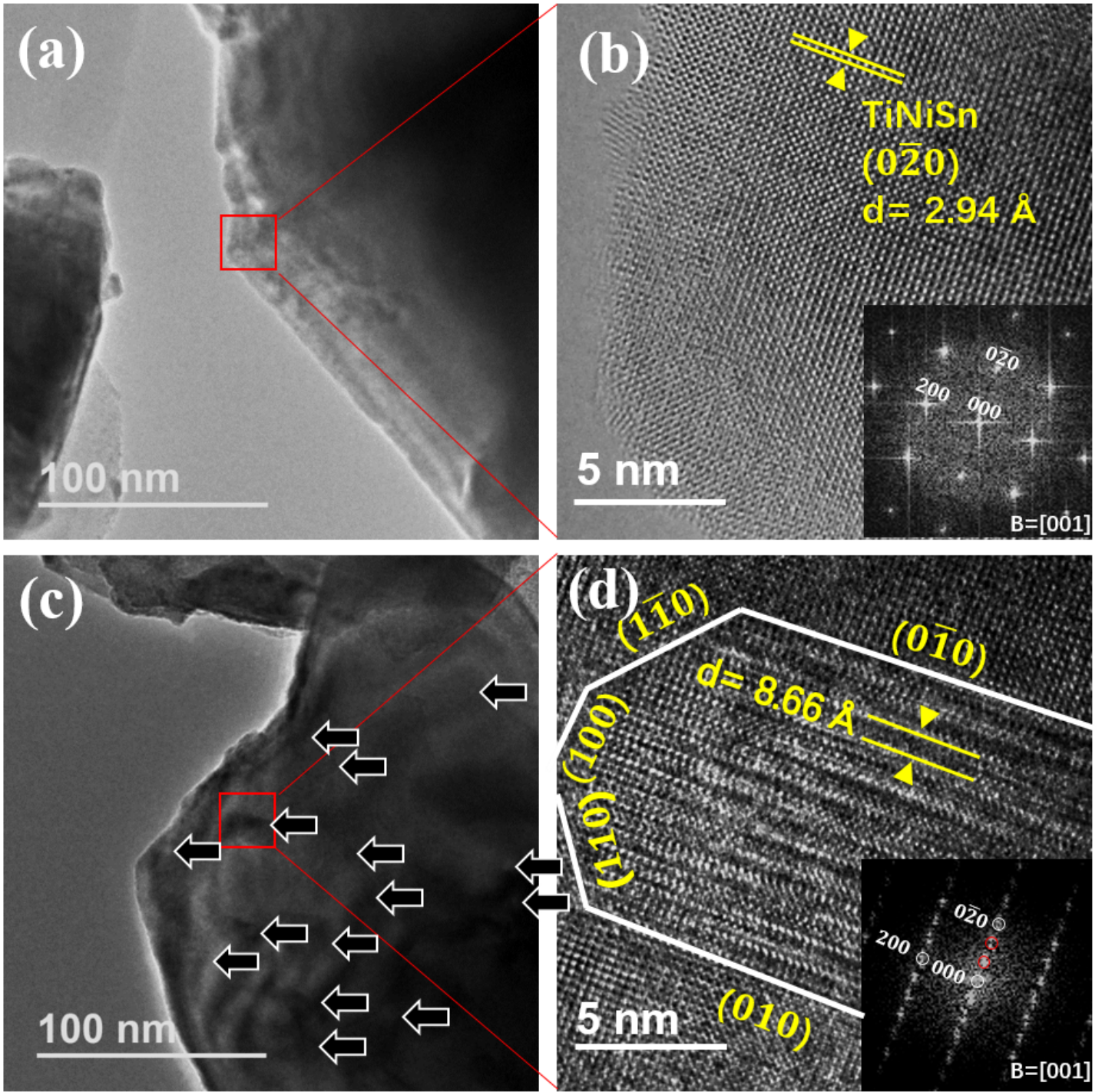


Figure 3

(a) TEM and (b) HRTEM images of TiNiSn, the insets are corresponding to the fast Fourier transformation (FFT) patterns of the matrix; (c) TEM and (d) HRTEM images of TiZr_{0.015}NiSn, the inset is FFT pattern of the nanodomain.

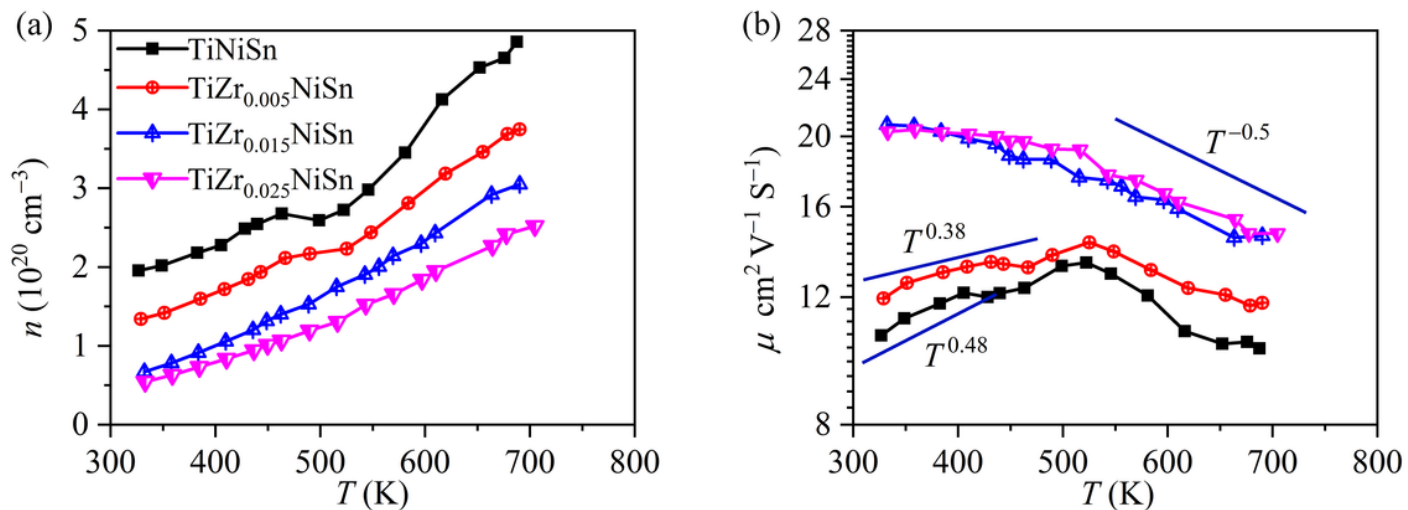


Figure 4

(a) Temperature-dependent Hall carrier concentration and (b) mobility of the samples TiZr_xNiSn ($x = 0, 0.005, 0.015, 0.025$).

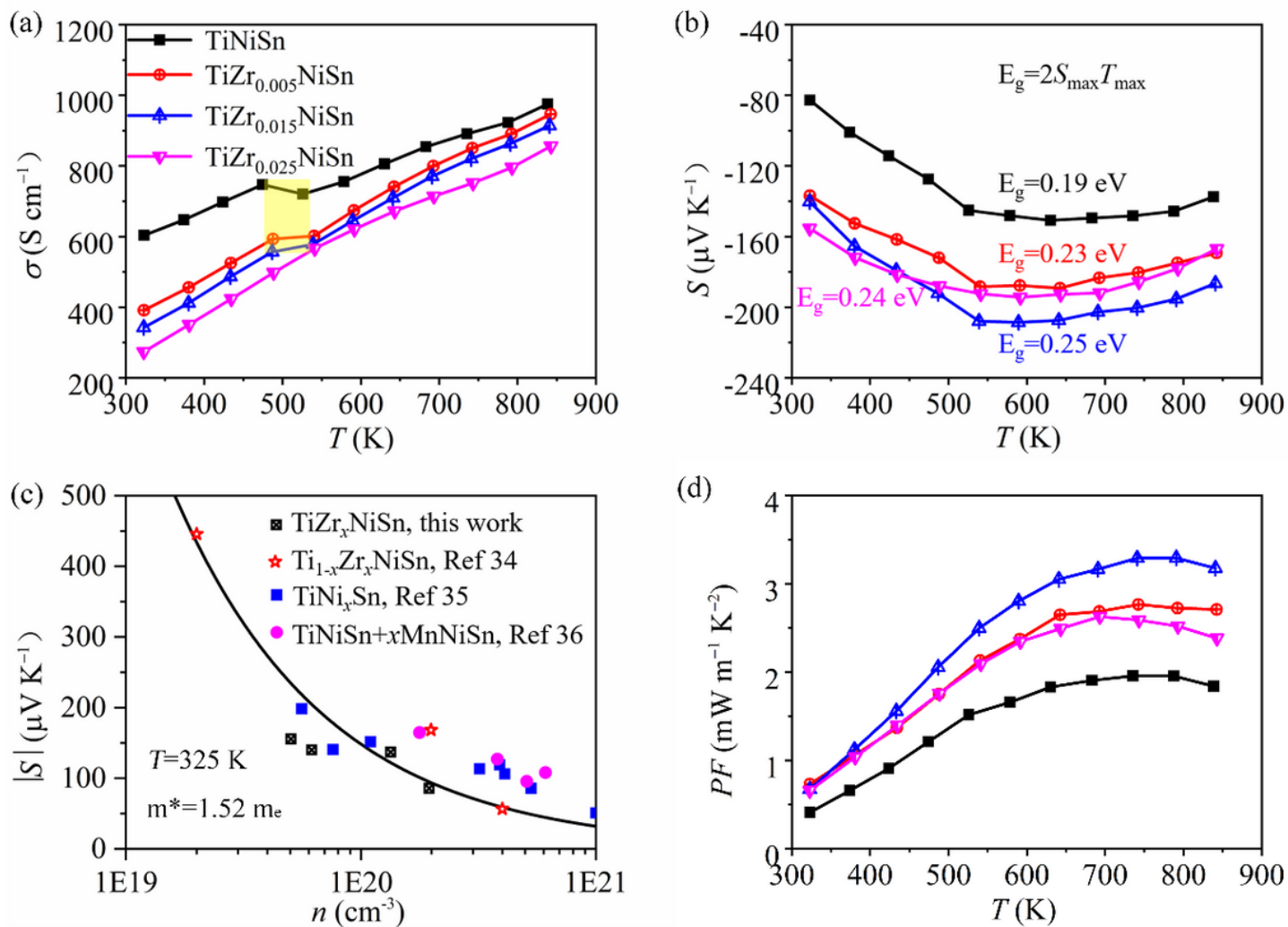


Figure 5

Temperature-dependent electrical properties of the samples TiZr_xNiSn ($x = 0, 0.005, 0.015, 0.025$); (a) electrical conductivity; (b) Seebeck coefficient; (c) Seebeck coefficient as a function of carrier concentration at 323 K; (d) power factor.

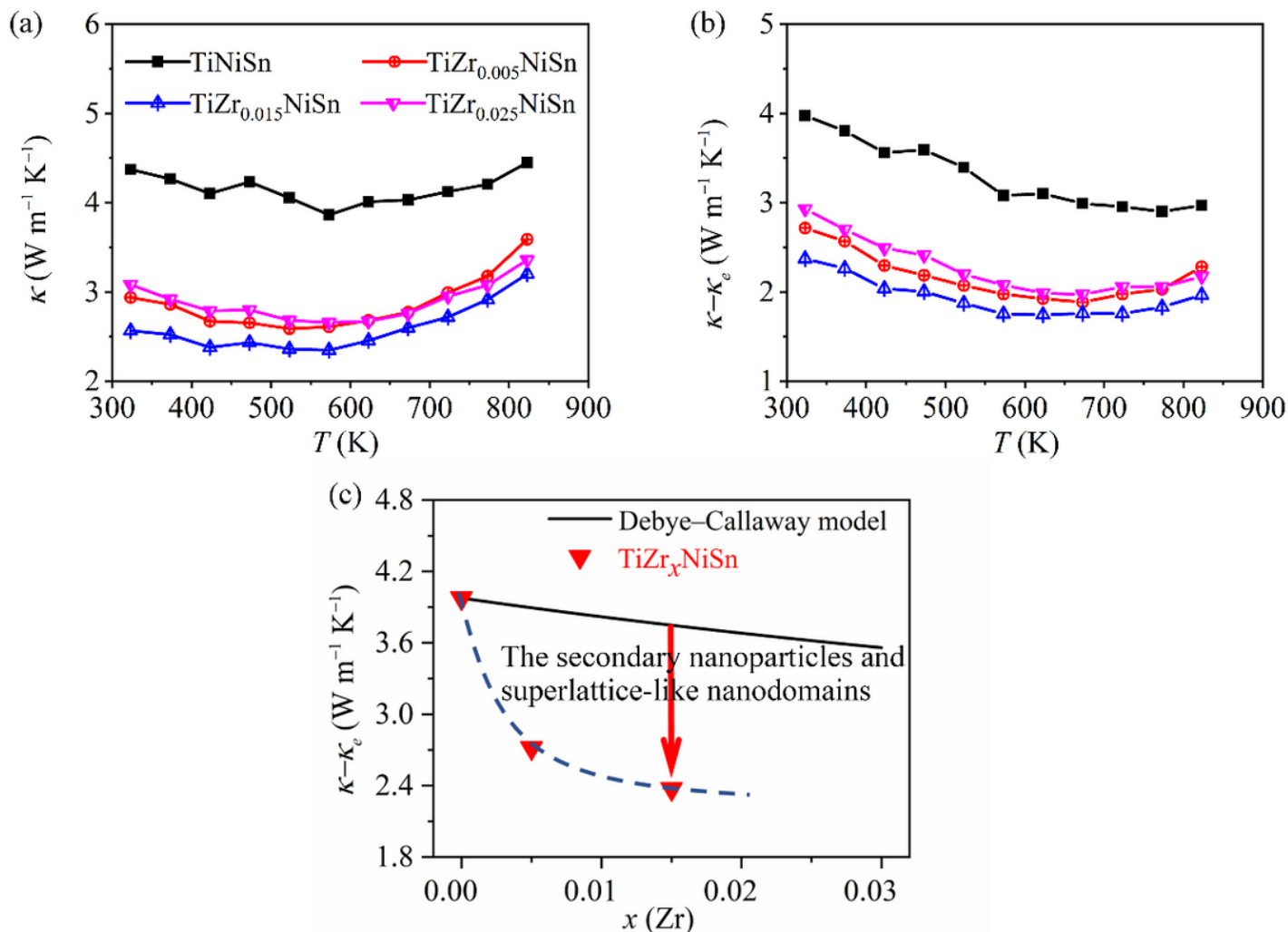


Figure 6

Temperature-dependent thermal properties of the samples TiZr_xNiSn ($x = 0, 0.005, 0.015, 0.025$): (a) total thermal conductivity; (b) lattice thermal conductivity; (c) The change trend of lattice thermal conductivity with Zr content at 323 K. The solid line represents fitting curve using the Debye-Callaway model.

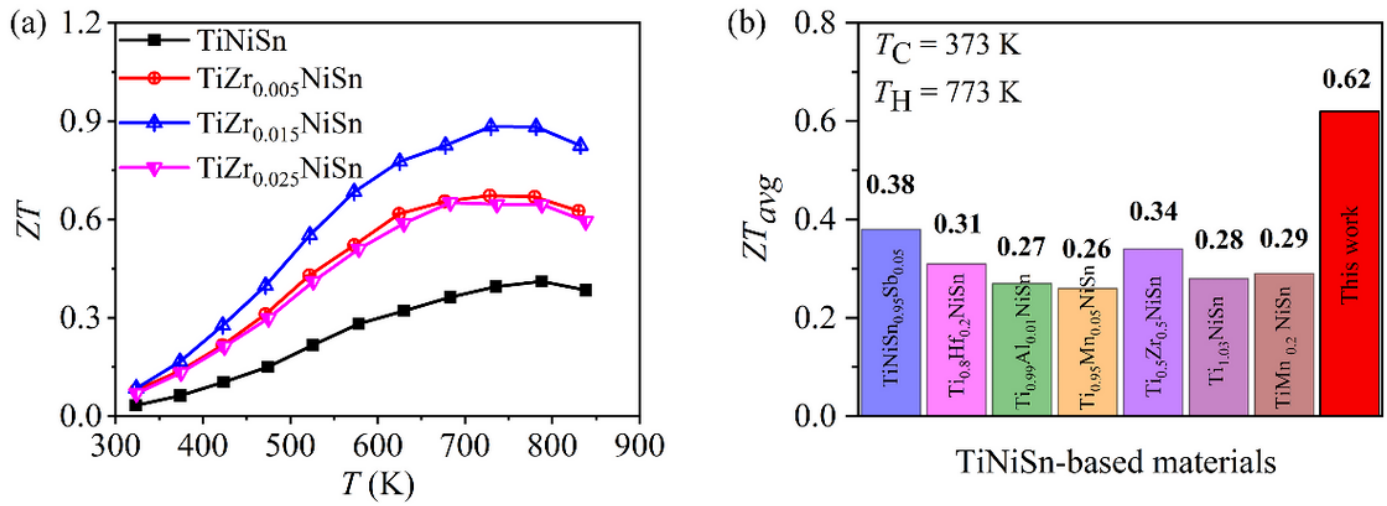


Figure 7

(a) Temperature-dependent of ZT values for the samples TiZrxNiSn. (b) The comparison of the average ZT value of TiNiSn-based materials obtained in this work with the literatures [14,15,24,42–44].

Supplementary Files

This is a list of supplementary files associated with this preprint. Click to download.

- [JACSupplementaryMaterial20210714.docx](#)